eprints@whiterose.ac.uk
https://eprints.whiterose.ac.uk/

Accepted Manuscript

Title: The effects of ultrasonic treatments on the microstructure and mechanical properties of SAC0307 solder

Author: Haiyan Chen Ziliang Chen Zhenmin Lai Yi Li Li Guo

Please cite this article as: Haiyan Chen, Ziliang Chen, Zhenmin Lai, Yi Li, Li Guo, The effects of ultrasonic treatments on the microstructure and mechanical properties of SAC0307 solder, <![CDATA[*Journal of Materials Processing Tech.*]]> (2018), https://doi.org/10.1016/j.jmatprotec.2018.11.025

The effects of ultrasonic treatments on the microstructure and mechanical properties of SAC0307 solder

Haiyan Chen[a], Ziliang Chen[a], Zhenmin Lai[a], Yi Li[b,*], Li Guo[c]

[a]*School of Material and Energy, Guangdong University of Technology, Guangzhou, China, 510006*
[b]*School of Mathematics and Statistics, University of Sheffield, Hicks Building, Hounsfield Road, Sheffield, UK, S3 7RH*
[c]*Stannum Industry Co. Ltd, Huizhou, Guangdong, China, 516123*

Abstract

The microstructures and physical properties of SAC0307 lead-free solder formed by an ultrasound-assisted semi-solid casting process were analyzed. The damages to a thin aluminium foil placed in the alloy melt at 226°C showed strong effects of acoustic streaming. Significant erosion due to cavitation was found for powers higher than 450W. Numerical simulations of a collapsing cavitation bubble obtained the highest peak pressure and temperature when the ultrasonic power was around 550W. When the ultrasonic power was between 500W and 600W, sub-grains were observed and the crystal grains became equiaxed with the smallest average grain size of about 140μm. The highest tensile strength found in this range was about 36.6 MPa. The density was 7.35g/cm^3. The elongation at break was about 60%, which was 40% higher than the value obtained by traditional casting techniques.

Keywords: Lead-free solder, metal casting, ultrasonic treatments,

*∗Corresponding author
Email addresses:* gdutchy1@163.com (Haiyan Chen), yili@shef.ac.uk (Yi Li)

cavitation, bubble dynamics

1. Introduction

Past research has shown that applying ultrasonic treatments (UTs) in the casting process can modify the micro-structure and effectively improve the physical properties of the alloys. The research has so far mainly focused on aluminum and magnesium alloys. In Jian et al. (2005), UTs were applied to A356 aluminium alloy. Under reported conditions, the typical size of the alloy grains was decreased from a few millimeters to around 200μm. In Das and Kotadia (2011), UTs was applied to LM6 aluminium alloy at 750°C. The average diameter of α-Al was reduced from 1500μm to 60μm, while the average length of the eutectic silicon decreased from 55μm to 8μm. UTs was applied in Xue et al. (2016) to Mg-6Zn-0.5Y-2Sn alloy. The thick dendritic α-Mg grains were turned into equiaxed grains after the UTs. The continuous thick secondary phase became discontinuous, finer in sizes, and homogenized. Compared with the alloy without UTs, the tensile yield strength, the ultimate tensile strength, and elongation at break were all significantly increased. Similar research was reported in Jiang and Wang (2015) and Zhang et al. (2012), among others. In comparison, the effects of UTs on Sn-based lead-free solder alloy have seldom been investigated. UTs with powers up to 267W were applied to SAC305 lead-free solder in Ji et al. (2014) at 238°C. Different cooling rates were examined. It was discovered that the size of the β-Sn grains decreased from 300μm to 20μm.

Grain refinement obtained in UTs is due to enhanced heterogeneous nucleation, while the latter comes from the combined effect of transient cavitation and acoustic streaming (Abramov, 1994; Eskin and Eskin, 2015). The high pressure pulses generated by collapsing cavitation bubbles and the shear stress due to acoustic streaming break down dendrites. The acoustic streams distribute the fragments in the melt. In the meantime, the high pressure

2

pulses increase the undercooling. These several physical processes all tend to increase the heterogeneous nucleation rate. However, the quantitative details depend on the alloy and the parameters of the UTs. A comprehensive quantitative investigation of cavitation-aided grain refinement in aluminium alloys was reported in Atamanenko (2010). No similar study for lead-free solder alloy has been reported.

The currently popular lead-free solders (e.g., Sn96.5Ag3Cu0.5, Sn95.5Ag3.8Cu0.7, and Sn95.5Ag3.9Cu0.6) have excellent physical properties. However, these solders are very expensive due to the high cost of Ag. The high cost has impeded the development of lead-free alloys for electronic soldering. Hypoeutectic solders have been researched as an alternative because of their low Ag contents. However, the solid-liquid phase lines of hypoeutectic materials usually span a wide interval ($8 \sim 10$ °C). The microstructures of the alloys often contain dendritic primary β-Sn phase and sheet-like Ag_3Sn metal composite. As a consequence, current hypoeutectic solder alloys suffer from low plasticity (Cheng et al., 2011), which has been an obstacle for efficient mass production. Improving the microstructure and physical properties of the alloys is the key to increase the appeal of hypoeutectic solders.

To suppress the segregation of the primary phase and increase the diffusion of the alloy elements, current research has mostly focused on adding suitable metal elements (Kanlayasiri and Sukpimai, 2016). Few attempts have been made to achieve the same effects by UTs. To fill this gap, this paper reports an experimental investigation on the effects of UTs on the casting of SAC0307 alloy. Different temperatures and ultrasonic powers were tested to identify the optimal operation conditions. The ultrasonic powers considered in this paper extended beyond the range covered in Ji et al. (2014). Non-monotonic dependence on the ultrasonic power was discovered. To explain the findings, the effects of acoustic cavitation and acoustic streaming were studied experimentally and by numerical simulations of cavitation bub-

3

bles. Experimentally, the erosion of sub-merged Aluminium foils was used to visualize the cavitation effects. This method is supplementary to those based on pressure measurement using cavitometers (Eskin and Eskin, 2015; Puga et al., 2011). The investigation provides additional understanding of the mechanisms of the UTs as well as valuable guidance to the application of the ultrasound assisted casting techniques.

2. Experimental materials and methods

2.1. The composition of the SAC0307 solder

The experimental material was the SAC0307 solder. The alloy contained 0.307 wt% Ag, 0.667 wt% Cu, 0.0015 wt% Fe, 0.0082 wt% Sb, 0.00024 wt% Al, and 0.006 wt% Ti, and the rest was Sn.

2.2. Experimental methods
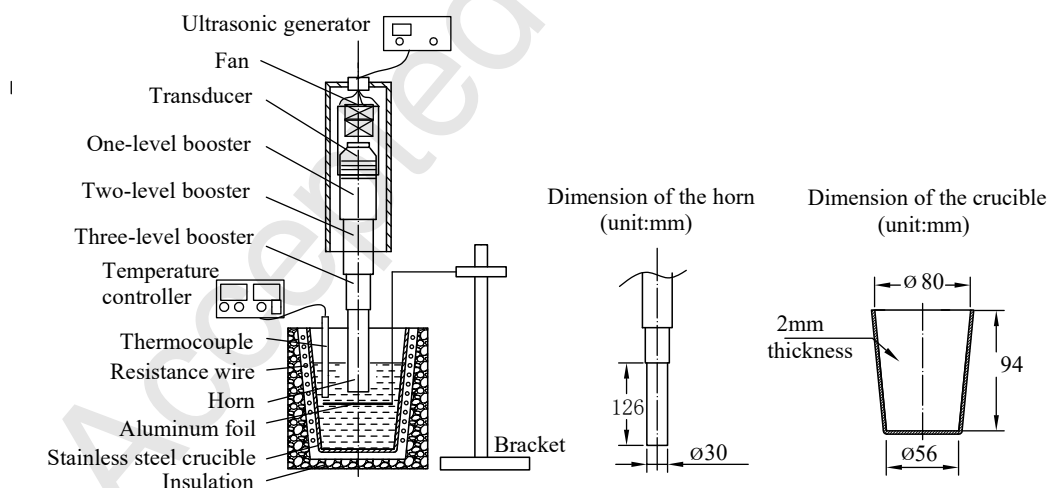
Figure 1: A schematic diagram for the experimental setup.

A schematic diagram for the experimental setup is shown in Fig. 1. A proprietary ultrasonic generator was used. The designed working frequency was fixed in the range from 19.70KHz to 20.10KHz. Screws and bolts were

4

used to connect the transducer, the boosters and the horn. The cylindrical horn was made of Ti6Al4V, with the diameter being 30mm and the length being 126mm. An aluminium foil was used to capture the effects of acoustic streaming and ultrasound-induced cavitation. The aluminium foil was placed in the crucible together with the solder and held in position by the bracket. The SAC0307 solder was heated up to 240°C, and left to cool down to 220°C, 226°C, 230°C, and 238°C, respectively. The temperature of the melt was then kept constant. The horn of the sonotrode was heated up to the same temperature and partially submerged in the melt so that the horn was 20mm above the aluminium foil. The ultrasonic generator was then switched on for 150 seconds, after which the aluminium foil was retrieved and analyzed. The erosion of the foil was quantified as evidence of the intensity of cavitation and acoustic streaming. Nine sets of experiments were conducted with the ultrasonic power being 0, 300, 400, 450, 500, 550, 600, 700 and 800W, respectively. The ultrasonic pressure at the location where the foil was placed was measured by an ultrasonic pressure sensor (UEC200A). The values were converted to the pressure inside the melt (Ying, 1990), and were used in the numerical simulations of the cavitation bubbles.

2.3. Method of casting

The alloy was prepared by the same experimental setup shown in Fig. 1, except that the aluminium foil was removed. UTs with the same parameters were applied in exactly the same way for 150 seconds. After the UTs, the melt was poured into a stainless steel mould equipped with cooling water channels, and solidified by water-cooling.

2.4. Methods of testing the samples

The samples were sanded with 500, 800, 1000, and 1500 grits sandpapers, respectively, and then polished and corroded with a 10% hydrochloric acid-methanol solvent. The microstructures of the processed samples were

5

examined with optical microscopes (Leica dmi8) and field emission scanning electron microscopes (Hitachi S-3400N). The average diameter and roundness of the crystal grains were calculated from more than ten images of the samples using the image-analysis software ImageJ (version 1.6r). The average diameter D and roundness R_n are defined by (Thomas et al., 2006)

$$D = 2\sqrt{A/\pi} \tag{1}$$

and

$$R_n = \frac{4\pi A}{P^2}, \tag{2}$$

where A is the area of the grain (μm^2), and P is the circumference (μm). A and P are obtained from ImageJ.

The densities of the samples were measured with the Archimedes method. The mechanical properties of the samples were measured according to the BS EN ISO 6892-1:2009 standard with a WAW-300B computer controlled micro-servomotor universal testing machine (BS EN ISO 6892-1, 2009). The stretching speed was 20mm/min. A Q2000 differential scanning calorimetry (DSC) was used to measure the alloy's melting parameters. The temperature was increased at a rate of 10°C/min, from 100°C to 300°C, with Nitrogen as the protection gas.

3. Results and discussion

3.1. The temperature for the ultrasonic treatments

To find the optimal temperature to apply the UTs, 550W UTs were applied for 150 seconds at 222°C, 226°C, 230°C, and 238°C, respectively. At different temperatures, the fraction of the solid phase in the alloy melt is different. The fraction was calculated according to the Speil formula (Yu and Jiang, 1990) and plotted in Fig. 2. When UTs were applied, the fraction of the solid phase was 88wt%, 66wt%, 8wt%, and 0wt% at the four temperatures, respectively. Images of the microstructure of the alloy obtained at

6
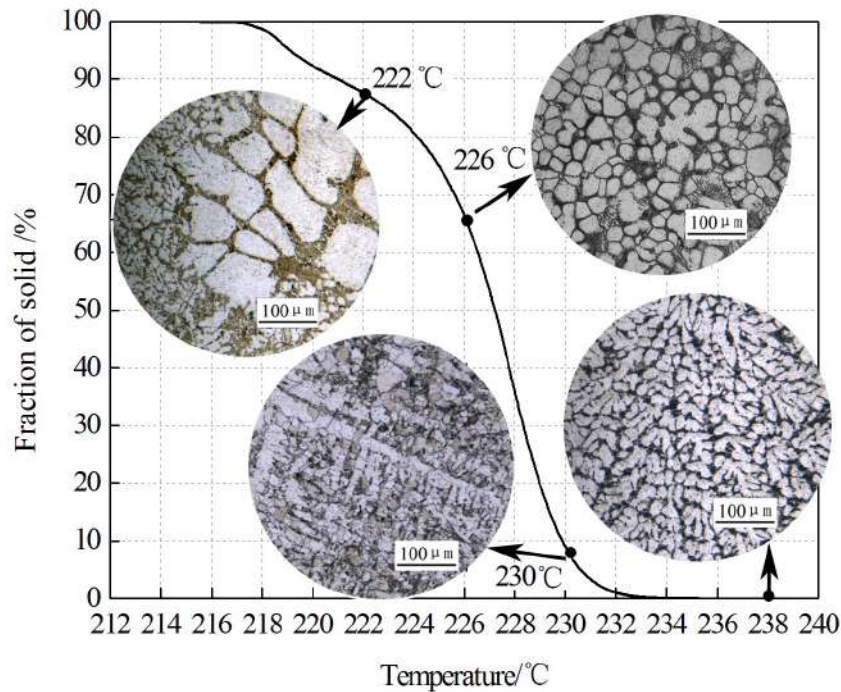
Figure 2: Fraction of the solid phase in the alloy melt as a function of temperature and the microstructure at four temperatures.

these temperatures are also shown in Fig. 2. At 222°C, the alloy displayed a mixture of equiaxed and dendritic grains. At 226°C, the microstructure consisted of uniform and equiaxed grains. At 230°C and higher temperatures, the microstructures mainly consisted of dendritic grains, same as in untreated alloy. Overall, the best outcome was achieved at 226°C for this ultrasonic power.

The improvements obtained at 226°C were due to transient cavitation and acoustic streaming induced by UTs (Abramov, 1994; Eskin and Eskin, 2015). At 222°C, the ultrasonic pressure decayed quickly due to the high fraction of the solid phase (88wt%). At 230°C and above, the solid phase

7

was less than 10wt%, leading to lower fragment concentration and weaker heterogeneous nucleation. In both cases, the effects of the UTs were limited.

3.2. The effects of the ultrasonic treatments

(a) 0W (b) 300W (c) 400W

(d) 450W (e) 500W (f) 550W

(g) 600W (h) 700W (i) 800W
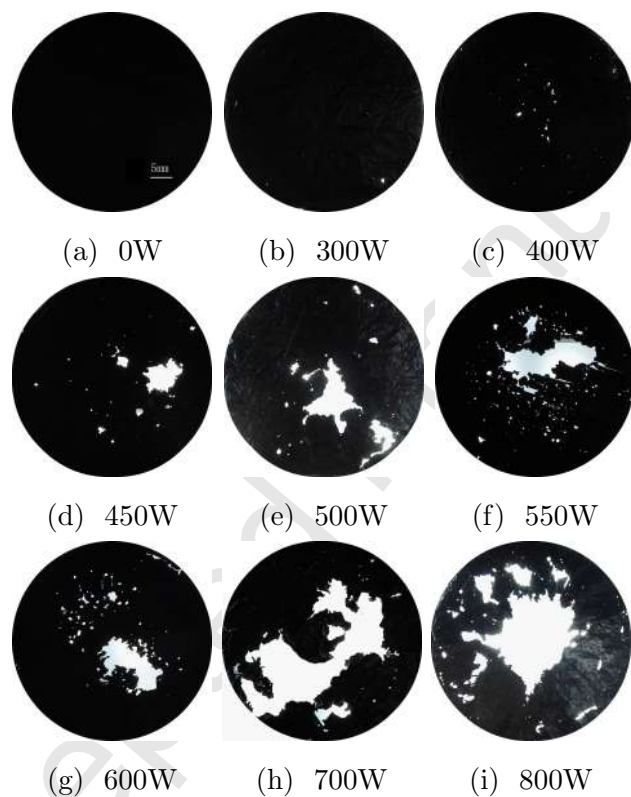
Figure 3: The images of the aluminium foils after UTs with different powers.

Fig. 3 shows the images of the aluminium foils after UTs with different powers had been applied. The image in Fig. 3(a) corresponds to the case without UTs, which shows no damage at all. When the power was 300W, a small number of circular micro-pores emerged, as shown in Fig. 3(b). The average diameter of the micro-pores was 200μm. The small sizes suggest that the pores were produced by collapsing cavitation bubbles, which provided indirect evidence of the transient cavitation in the molten alloy. Collapsing

8
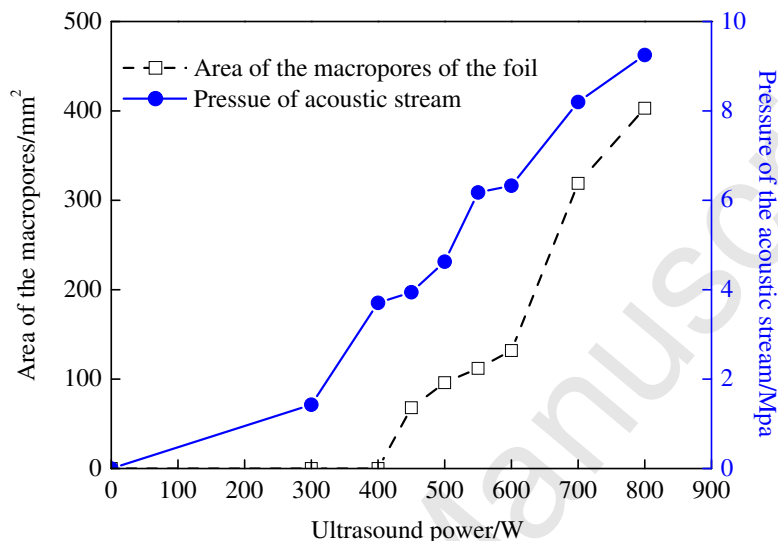
Figure 4: The area of the macro-pores and the pressure.

bubbles generated high speed high pressure micro-jets and high temperature spots. The former could puncture the foil, while the latter could lead to erosion on the foil. Large numbers of micro-pores are observed in Fig. 3(f) and (g), while large continuous areas of damage were also present. Therefore, both strong acoustic streaming and strong cavitation happened at 550W and 600W. When the power was 700W or 800W, the foils were badly damaged by acoustic streaming, to the extent that it was impossible to assess the effects of cavitation. The area of the macro-pores and the ultrasonic pressure are shown in Fig. 4 for different powers. The curves show that the strength of acoustic streaming increased monotonically. Because the effects from transient cavitation and acoustic streaming were mixed together, the effects of cavitation had been further investigated by numerical simulations.

9

3.3. Numerical simulations of cavitation bubbles

Cavitation bubbles are typically very small, hence remain essentially spherical. Assuming that the radius of a bubble is $R(t)$ at time t, the evolution of $R(t)$ can be modelled by the classical Keller-Miksis equation (see, e.g., (Brennen, 1995; Hunt and Jackson, 1966):

$$\left(1 - \frac{\dot{R}}{c}\right) \dot{R}\ddot{R} + \frac{3}{2}\left(1 - \frac{\dot{R}}{3c}\right)\dot{R}^2 = \left(1 + \frac{\dot{R}}{c}\right)\frac{P - P_\infty}{\rho} + \frac{R}{\rho c}\frac{d(P - P_\infty)}{dt}, \quad (3)$$

where $\dot{R}$ and $\ddot{R}$ are, respectively, the first and second derivatives of R with respect to t, ρ is the density of the liquid metal, c is the speed of sound in the liquid alloy, P is the pressure on the bubble, and P_∞ is the far field pressure. P is given by

$$P = \left(P_0 + \frac{2\sigma}{R_0}\right)\left(\frac{R_0}{R}\right)^{3\gamma} - \frac{2\sigma}{R} - \frac{4\mu\dot{R}}{R}, \quad (4)$$

where P_0 is the static pressure, R_0 is the equilibrium radius, σ is the surface tension coefficient, and μ is the dynamical viscosity of the liquid. It is assumed the gas in the bubble undergoes a polytropic process with exponent γ. P_∞ is given by

$$P_\infty = P_0 - P_A \sin(2\pi f t), \quad (5)$$

where f and P_A are, respectively, the frequency and the amplitude of the ultrasound wave. P_A is given in Fig. 4.

Collapsing cavitation bubbles generate short pulses of high temperature and pressure locally due to the high speed collapsing bubble wall. Assuming adiabatic process, the maximum pressure and temperature of the gas in the bubble can be calculated from (Eskin and Eskin, 2015)

$$P_{\max} = \left(P_0 + \frac{2\sigma}{R_0}\right)\left(\frac{R_0}{R_{\min}}\right)^{3\gamma}, \quad (6)$$

and

$$T_{\max} = T_\infty \left(\frac{R_0}{R_{\min}}\right)^{3\gamma - 3}, \quad (7)$$

10

Table 1: Parameters used in Eqs. (3)-(7).

Parameter	Value	Parameter	Value
ρ	7030.92 kg/m^3	c	2462 m/s
R_0	2 μm	σ	0.5615 N/m
μ	2.3672×10^{-3}Pa·s	f	20 kHz
P_0	1.0201 MPa	γ	1.3871
T_∞	499.15K		

where $R_{\min}$ is the minimum bubble radius found in the simulations, $P_{\max}$ is the peak pressure inside the collapsing bubble, $T_{\max}$ is the maximum temperature in the bubble, and T_∞ is the temperature in the liquid metal far away from the bubble. Table 1 gives the values for the parameters in a Sn-0.3Ag-0.7Cu liquid alloy taken from Alcock et al. (1984); Shen and Wu (2012); Zhang and Zhao (1987). Using these parameters, Eqs. (3), (4) and (5) were solved with the self-adaptive fourth-order Runge-Kutta-Fehlberg method implemented in MATLAB. $P_{\max}$ and $T_{\max}$ were then calculated.

The results are shown in Fig. 5, which shows that $P_{\max}$ and $T_{\max}$ were the highest when the power was 550W. The localized high pressure, high temperature release had the following effects. Firstly, it led to strong pressure undercooling. According to the Clausius-Clapeyron equation, the pressure undercooling ΔT_m is given by (Yu et al., 2007; Jiang et al., 2015):

$$\Delta T_m = \Delta P \; T_m \; \frac{V_L - V_S}{\Delta H}, \tag{8}$$

where V_L and V_S are the volumes of the alloy in the liquid and solid states, respectively; T_m is the melting temperature when the pressure is 1atm; ΔH is the enthalpy change during the solidification, and ΔP is the change in system pressure. Since $V_L - V_S > 0$ for SAC alloy, pressure undercooling ΔT_m was increased when the collapsing bubble increased the system pressure.

11
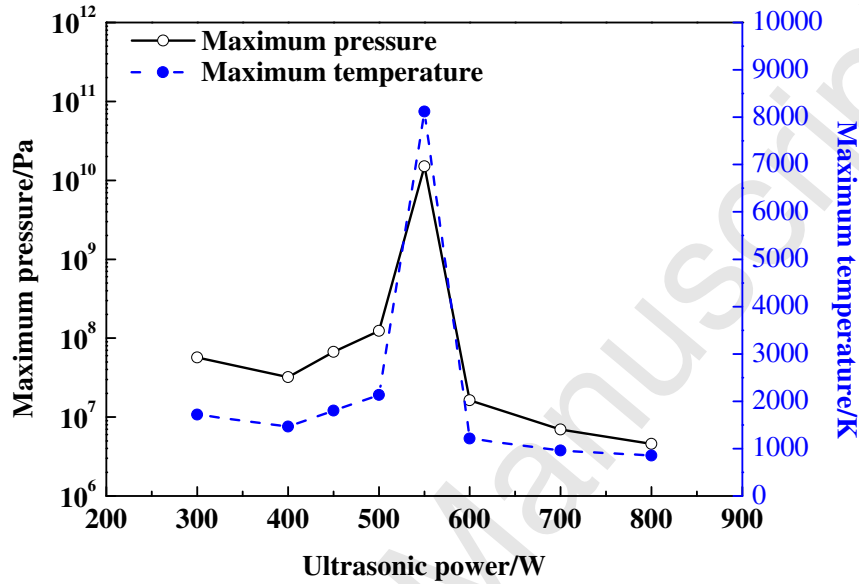
Figure 5: The maximum pressure and temperature in a collapsing bubble.

Secondly, the very high peak pressure and temperature helped fragment the crystallized dendrites. Both effects increased nucleation rate and eventually refined the alloy grains. This will be analyzed in the next section.

3.4. Microstructure

Fig. 6 shows the microstructures of the samples. The sizes and round-ness of the grains shown in Fig. 6 are plotted in Fig. 7. Fig. 6(a) shows the samples produced by traditional mechanical stirring without UTs. Fig. 6(b) is obtained with 300W UTs. The similarity in the two images show that UTs with power lower than 300W did not change the dendritic structure of the alloy. Result in Fig. 6(c) was obtained with 400W UTs. The primary struc-ture was still columnar dendrites, but the roots of the secondary dendrites had become thinner. The weakening at the roots could be explained by the periodic straining due to acoustic streaming (Hu et al., 2016). However, Fig.

12

(a) 0W

(b) 300W

(c) 400W

(d) 500W
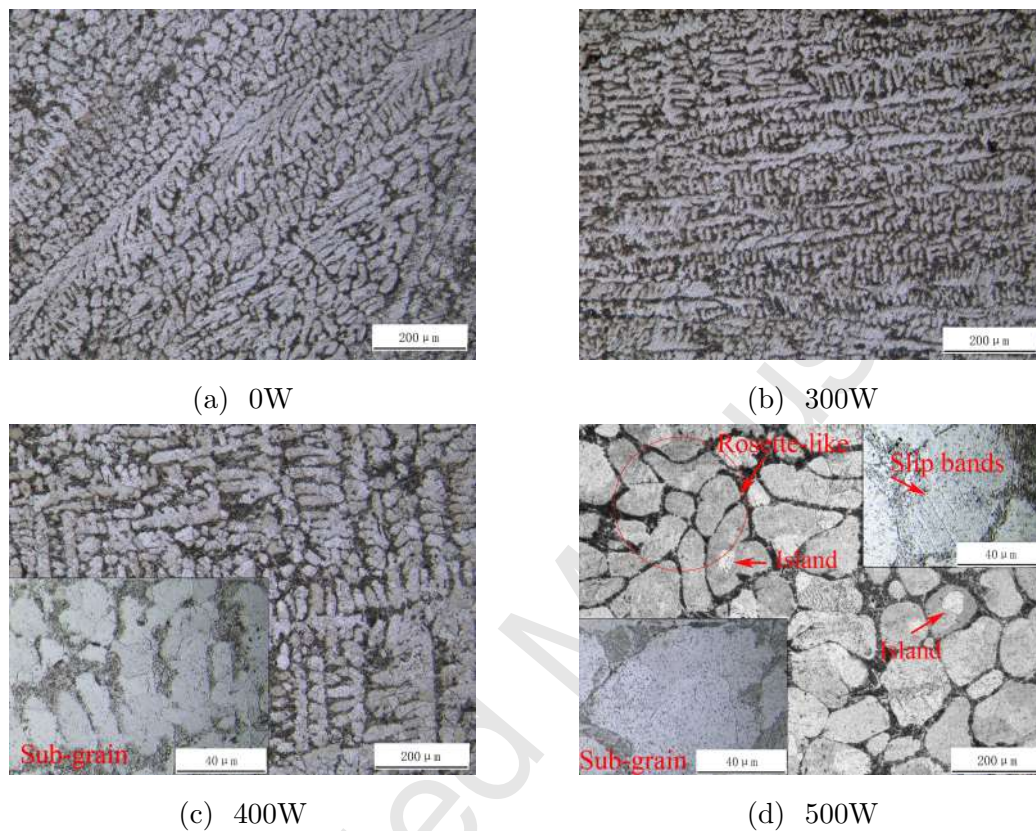
Figure 6: Continued on next page

3(c) indicates that transient cavitation had happened at this power. Therefore cavitation could contribute to the weakening too. In general, cavitation tends to occur first on the defects on a surface (Franc, 2005). Here, the roots of the secondary dendrites are such defects so that the cavitation bubbles tended to accumulate at the roots. The high-pressure re-entrant jets generated by the collapsing bubbles might impinge on the roots hence weakening them. Meanwhile, the high temperature generated from the collapses could also remelt the roots.

The average grain sizes at 550W and 600W were 142μm and 140μm, respectively, which are among the smallest for the powers considered, as shown

13

(e) 550W

(f) 600W

(g) 700W

(h) 800W
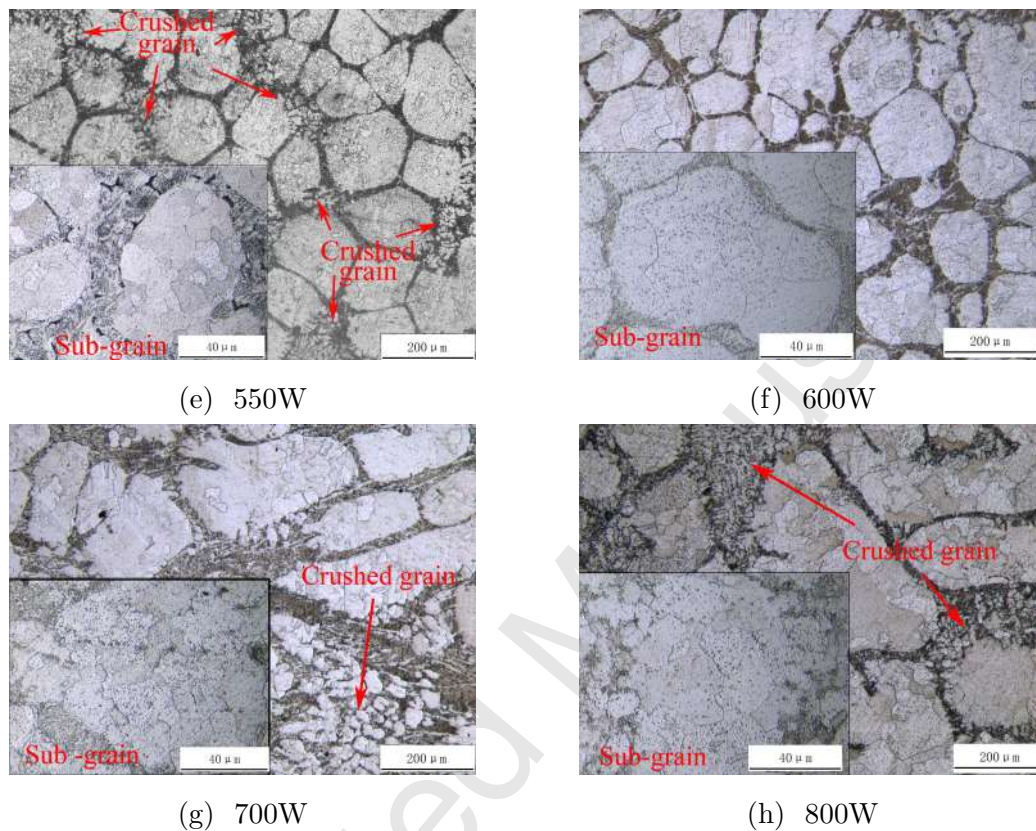
Figure 6: The optical microstructure of the alloy samples. The insets in (c)-(h) show the same samples at a higher resolution.

in Fig. 7. The roundness was 0.93 and 0.88, respectively. Fig. 6(e) and (f) show that the microstructures were mainly equiaxed crystal grains. These features were due to the joint effects of acoustic streaming and cavitation. These effects were both very strong for these powers (c.f. Fig. 3). The dendrites were broken off and dispersed uniformly in the melt. Acoustic streaming also led to more uniform temperature and concentration distributions. Fig. 5 shows that the pressure undercooling effect was also maximized at 550W. All these factors increased the heterogeneous nucleation rate, leading to finer grains. However, further increasing the power reversed the trend.

14
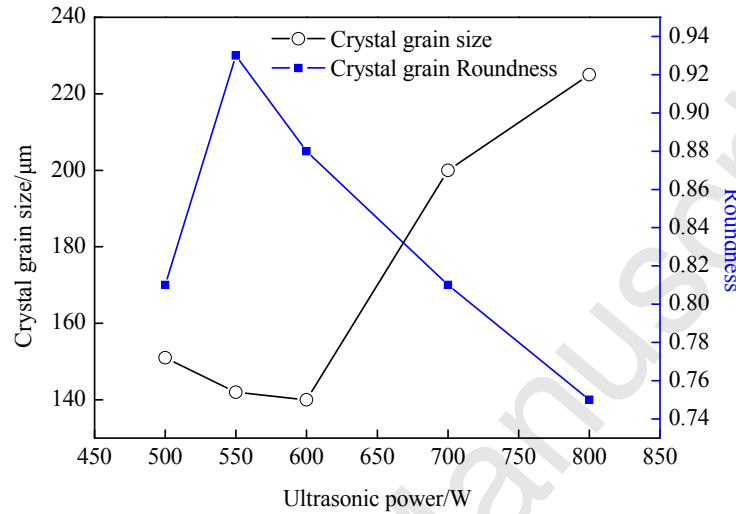
Figure 7: The size and roundness of the crystal grains.

For power higher than 600W, the average size of the grains increased with the power, while the roundness decreased. This observation is shown in Fig. 7, with corresponding microstructures given in Fig. 6(f)-(h). This behavior can be explained by two mechanisms. Firstly, the peak pressure due to cavitation was lower at these powers (as shown in Fig. 5). This led to lower under-cooling, hence lower nucleus formation rate and larger grain sizes. Secondly, the stronger acoustic streams at these powers gave rise to higher collision rate between the small grains. Thus it is more likely for smaller grains to conglomerate into larger ones (Hu et al., 2016).

The bottom left insets in Fig. 6(c)-(h) highlight the sub-grains structures in the samples. These areas represent equiaxed sub-grains embedded in larger crystallites. A clear evidence of the slip bands is shown in the top-right inset in Fig. 6(d), where they appear as clearly distinguishable, parallel, steps-like structures.

The microstructures of the alloy sample treated by 550W ultrasounds

15
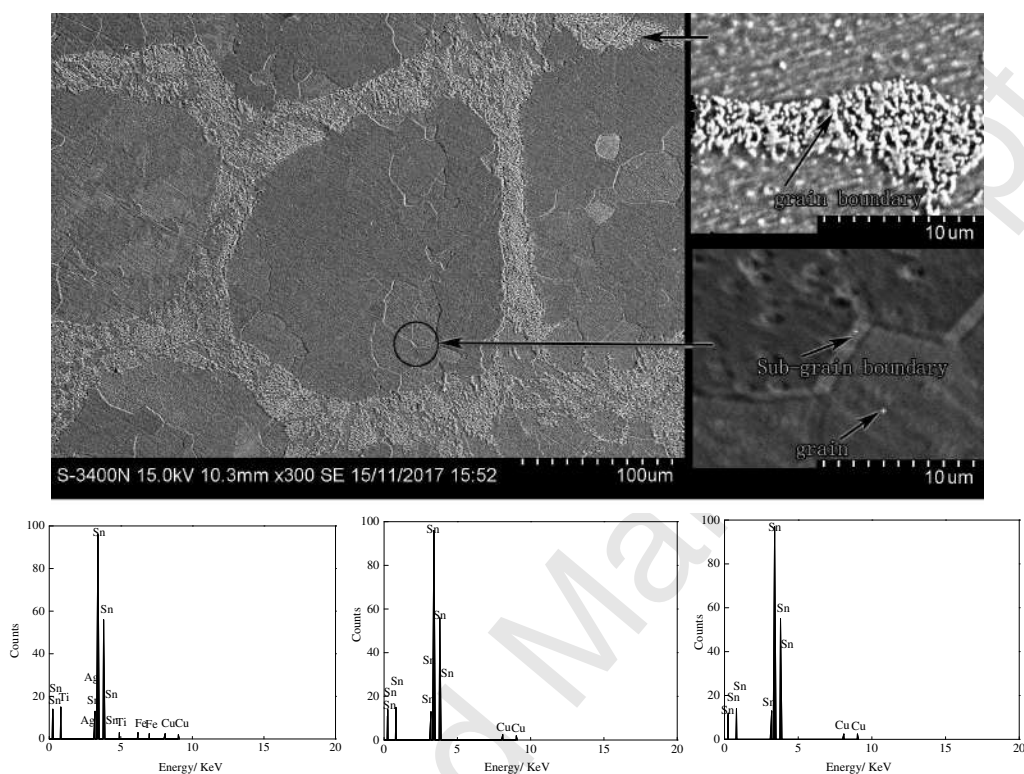
Figure 8: SEM spectroscopy of the alloy samples treated with 550W ultrasounds. The bottom figures correspond to (from left to right): grain boundaries, sub-grain boundaries, and grain interior, respectively.

were also analyzed with SEM. The results are shown in Fig. 8 and Table. 2. Fe and Ti, as impurity elements, had high concentrations on the boundaries between the crystal grains. Significant amounts of alloy elements Cu and Ag were also found on the grain boundaries. The two elements tend to form chemical composites Cu_6Sn_5 and Ag_3Sn with Sn. Table 2 shows that the concentrations of the alloy elements in the interior of the grains and on the boundaries of the sub-grains were about the same. On both locations, only a small amount of Cu was found while no Ag was detected.

Under the straining induced by acoustic streaming, the crystal grains were deformed continuously, which increased the dislocation density and the

16

Table 2: Chemical compositions at different locations (wt%).

Location	Ti	Fe	Cu	Ag	Sn
Grain boundaries	0.05	0.478	0.875	12.113	86.535
Sub-grain boundaries	0	0	0.612	0	99.388
Grain interior	0	0	0.653	0	99.347

number of slip bands. Different slip bands joined together to form 'islands'. The islands were separated by densely packed dislocation 'walls' (Li et al., 2008). This feature is shown clearly by the top-right panel in the upper part of Fig. 8. The interior of the islands, where the dislocation density was lower, constituted sub-grains. The 'walls', where dislocations intertwined and interlocked, formed the sub-grain boundaries. Sub-grain boundaries improved the strength and plasticity of the alloy by resisting the movement of dislocations.

3.5. Mechanical properties
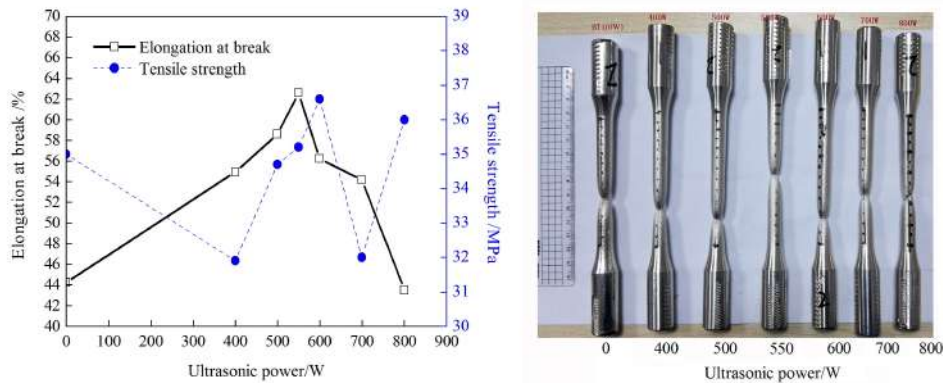
Figure 9: Elongation at break and tensile strength (left) and the image of the samples at the breaking point (right).

The mechanical parameters of the SAC0307 solder obtained with UTs are summarized in Table 3 and Fig. 9. The elongation at break reached the max-

17

Table 3: The density ρ of the alloy samples.

Ultrasonic power (W)	0	400	500	550	600	700	800
ρ (g/cm³)	7.30	7.33	7.35	7.34	7.32	7.32	7.32

imum value 62% at 550W, which is 41.53% higher than the value obtained without UTs. At 550W, the strength was 35.2MPa, which is larger than the value when no UT was used (35MPa). The highest strength, 36.6MPa, was found at 600W, which was an 4.5% improvement.

The above results are the consequences of the two distinctive features of the microstructures of the samples, shown in Fig. 7 and Fig. 8. At 550W, the crystal grains were rounder and finer, which led to more uniform strain distribution, hence delayed breaking. Sub-grains were also observed at this power. The interlocking sub-grain boundaries blocked the movement of dislocations, hence significantly improved the plasticity of the alloy.

The density of the alloy is given in Table 3. The data show that UTs increased the density of the alloy. The largest increase (0.7%) was found at 500W. The change in density is due to the degassing effect of the UTs. The results in Table 3 were obtained at 226°C. Since the degassing effect was not the main focus of this study, the results at other temperatures were not explored, although more efficient degassing could be achieved with a higher over-heating.

4. Conclusions

1. The optimal ultrasonic power was in the range from 500W to 600W for the 226°C SAC0307 semi-solid alloy melt. The best elongation of the alloy reached about 60% in this range, the tensile strength reached 36.6MPa and the density was 7.35g/cm³. The crystal grains of the alloy changed from dendritic to equiaxed with diameter approximately

18

140μm.

2. Strong acoustic streaming was captured. Acoustic streaming led to more uniform temperature and concentration distributions and enhance heterogeneous nucleation. It induced periodic straining and generated sub-grain structures. At higher powers, the acoustic streams could increase collision between dendritic fragments and lead to larger grains.

3. The evolution of cavitation bubbles were modelled by the classical Keller-Miksis equation. Simulations found the highest pressure and temperature pulses generated by collapsing bubbles at 550W. The high pressure and high temperature enhanced heterogeneous nucleation and refined the grain sizes.

5. Acknowledgements

Z. Hu, X. Li, H. Yan, X.-Q. Wu, H. Qun, and J.-W. Lin, 2016. Effects of ultrasonic vibration on microstructure evolution and elevated-temperature mechanical properties of hot-extruded Mg-6Al-0.8Zn-2.0Sm wrought magnesium alloys. J. Alloys Compd. 685, 58–64.

A. Das, H. R. Kotadia, 2011. Effect of high-intensity ultrasonic irradiation on the modification of solidification moicrostructure in a Si-rich hypeutectic Al-Si alloy. Materials Chemistry and Physics 125, 853–859.

BS EN ISO 6892-1, 2009. Metallic materials. Tensile testing. Method of test at ambient temperature.

19

C. B. Alcock, V. P. Itkin, and M. K. Horrigan, 1984. Vapour pressure equations for the metallic elements: 298-2500K. Canadian Metallurgical Quarterly 23, 309–313.

C. B. Lee, I. Y. Lee, S. B. Jung, and C. C. Shur, 2002. Effect of surface finishes on ball shear strength in BGA joints with Sn-3.5 mass% Ag solder. Mater. Trans. 43, 751–756.

C.-K. Jen, J.-F. Moisan, C.-Q. Zheng, C.-A. Loong, S. E. Kruger, M. T. Shehata, and E. Essadiqi, 2004. In-line ultrasonic monitoring of semi-solid magnesium die casting process. Ultrasonics 41, 777–784.

E. C. Brennen, 1995. Cavitation Bubble Dynamics. New York: Oxford University Press.

J. B. Keller and M. Miksis, 1980. Bubble oscillations of large amplitude. J. Acoust. Soc. Am. 68, 628–633.

A. Prosperetti and A. Lezzi, 1986. Bubble dynamics in a compressible liquid. Part 1. First-order theory. J. Fluid Mech. 168, 457–478.

E.-J. Baek, T.-Y. Ahn, J.-G. Jung, J.-M. Lee, Y.-R. Cho, and K.-J. Euh, 2017. Effects of ultrasonic melt treatment and solution treatment on the microstructure and mechanical properties of low-density multicomponent $Al_{70}Mg_{10}Si_{10}Cu_5Zn_5$ alloy. J. Alloys Compd. 696, 450–459.

F. Gao, T. Takemoto, and H. Nishikawa, 2006. Morphology and growth pattern transition of intermetallic compounds between Cu and Sn-3.5Ag containing a small amount of additives. J. Electron. Mater. 35, 2081–2087.

F.-J. Cheng, F. Gao, J.-Y. Zhang, W.-S. Jin and X. Xiao, 2011. Tensile properties and wettability of SAC0307 and SAC105 low Ag lead-free solder alloys. J. Mater. Sci. 46, 3424–3429.

20

G. Y. Li, X. D. Bi, Q. Chen, and X. Q. Shi, 2011. Influence of dopant on growth of intermetallic layers in Sn-Ag-Cu solder joints. J. Electron. Mater. 40, 165–175.

H.-J. Ji and Q. Wang and M.-Y. Li and C.-Q. Wang, 2014. Effects of ultrasonic irradiation and cooling rate on the solidification microstructure of Sn-3.0Ag-0.5Cu alloy. J. Mater. Process. Tech. 214, 13–20.

H. S. Xue, Z. H. Xing, W. N. Zhang, G. Yang, F. S. Pan, 2016. Effects of ultrasonic treatment on microstructure and mechanical properties of Mg-6Zn-0.5Y-2Sn alloy. Trans. Nonferrous Met. Soc. China 26, 1826–1834.

J. Jiang and Y. Wang, 2015. Microstructure and mechanical properties of the semi-solid slurries and rheoformed component of nano-sized SiC/7075 aluminium matrix composite prepared by ultrasonic-assisted semi-solid stirring. Material science and engineering A 639, 350–358.

J. K. Hunt and K. A. Jackson, 1966. Nucleation of solid in an undercooled liquid by cavitation. J. Appl. Phys. 37, 254–257.

J.-P. Li, J. Shen, X.-D. Yan, B.-P. Mao, and L.-M. Yan, 2008. Effect of temperature on microstructure evolution of 7075 alloy during hot deformation. The Chinese Journal of Nonferrous Metals 18, 1951–1957.

J.-R. Zhang and Y.-T. Zhao, 1987. Manual of thermal physical properties of engineering materials (In Chinese). New age press.

K. Kanlayasiri and K. Sukpimai, 2016. Effects of indium on the intermetallic layer between low-Ag SAC0307-xIn lead-free solders and Cu substrate. J. Alloys Compd 668, 169–175.

L. C. Tsao, 2011. Suppressing effect of 0.5 wt% nano-TiO2 addition into Sn-3.5Ag-0.5Cu solder alloy on the intermetallic growth with Cu substrate during isothermal aging. J. Alloys Compd. 509, 8441–8448.

21

L. Zhang, D. G. Eskin, A. Miroux, and L. Katgerman, 2012. Role of solute and transition metals in grain refinement of aluminium alloys under ultrasonic melt treatment. In: Weiland H., Rollett A.D., Cassada W.A. (eds) ICAA13 Pittsburgh. , 1389–1394.

Q. Gao, S.-S. Wu, S.-L. Lu, X.-C. Xiong, R. Du, and P. An, 2017. Effects of ultrasonic vibration treatment on particles distribution of TiB2 particles re-enforced aluminium composites. Mat. Sci. Eng. A. 680, 437–443.

S. W. Jeong, J. H. Kim, and H. M. Lee, 2004. Effect of cooling rate on growth of the intermetallic compound and fracture mode of near-eutectic Sn-Ag-Cu/Cu pad: Before and after aging. J. Electron. Mater. 33, 1530–1544.

X. Jian, H. Xu, and T. T. Meek, 2005. Effect of power ultrasound on solidification of aluminum A356 alloy. Materials Letters 59, 190–193.

Z.-Y. Qin and H. Alehossein, 2016. Heat transfer during cavitation bubble collapse. Appl. Therm. Eng. 105, 1067–1075.

Z.-Z. Shen and S.-J. Wu, 2012. Dynamical behaviors of a bubble cluster under ultrasound field. Acta Phys. Sin. 61, 244301.

C.-F. Ying, 1990. Ultrasonics. Beijing: Science Press.

T. Thomas, X. G. Meek, H. H. Xu, and Q. Y. Han, 2006. Ultrasonic processing of materials. Oak Ridge: Oak Ridge National Laboratory TODO.

B. L. Yu and J. D. Jiang, 1990. Applied Thermal Analysis. Beijing: Textile Industry Press.

O. V. Abramov, 1994. Ultrasound in liquid and solid metals. Moscow: CRC press.

22

G. I. Eskin and D. G. Eskin, 2015. Ultrasonic treatment of light alloy melts, second edition. CRC Press.

H. Puga and J. Barbosa and J. Gabriel and E. Seabra and S. Ribeiro and M. Prokic, 2011. Evaluation of ultrasonic aluminium degassing by piezoelectric sensor. J. Mater. Process. Tech. 211, 1026-1033.

T. V. Atamanenko, 2010. Cavitation-aided grain refinement in aluminium alloys. Doctoral Thesis: Delft University of Technology.

A. Yu, S. P. Wang, N. Y. Li, and H. Hu, 2007. Pressurized solidification of magnesium alloy AM50A. J. Mater. Process. Tech. 191, 247-250.

W. Jiang, C. M. Zou, H. W. Wang, and Z. J. Wei, 2015. Modeling of eutectic spacing in binary alloy under high pressure solidification. J. Alloys Compd. 646, 636-667.

J. P. Franc, 2005. Fundamentals of Cavitation. New York: Kluwer Academic Publishers.

23

Figure captions

- **Fig** 1: A schematic diagram for the experimental setup.

- **Fig** 2: Fraction of the solid phase in the alloy melt as a function of temperature and the microstructure at four temperatures.

- **Fig** 3: The images of the aluminium foils after UTs with different powers.

- **Fig** 4: The area of the macro-pores and the pressure.

- **Fig** 5: The maximum pressure and temperature in a collapsing bubble.

- **Fig** 6: The optical microstructure of the alloy samples. The insets in (c)-(h) show the same samples at a higher resolution.

- **Fig** 7: The size and roundness of the crystal grains.

- **Fig** 8: SEM spectroscopy of the alloy samples treated with 550W ultrasounds. The bottom figures correspond to (from left to right): grain boundaries, sub-grain boundaries, and grain interior, respectively.

- **Fig** 9: Elongation at break and tensile strength (left) and the image of the samples at the breaking point (right).

24

Table captions

- **Table** 1: Parameters used in Eqs. (3)-(7).

- **Table** 2: Chemical compositions at different locations (wt%).

- **Table** 3: The density ρ of the alloy samples.

25